Oscillatory loading can alter the velocity rate dependence of ice-on-rock friction

Rob M. Skarbek[1], Christine McCarthy[2], and Heather M. Savage[3]

[1]Lamont-Doherty Earth Observatory
[2]Lamont-Doherty Earth Observatory, Columbia University
[3]UC Santa Cruz

November 22, 2022

Abstract

Rate and state frictional parameters are typically determined using two types of experimental protocols: velocity steps and slide-hold-slide events. Here we take a new approach by examining the frictional response to controlled, harmonic oscillations in load point velocity. We present a Matlab graphical user interface software package, called RSFitOSC, that allows users to easily determine frictional parameters by fitting oscillation events using the rate and state friction equations. We apply our new methods to a set of ice-rock friction experiments conducted over a temperature range of -16.4°C to -2°C, and described in a companion paper: McCarthy et al. (In Review). Values of the frictional stability parameter (a-b) determined from oscillations reveal dominantly velocity-weakening behavior across the entire range of experimental conditions. However, values of (a-b) determined from velocity steps in the same experiments yield velocity-strengthening behavior. We also show that the elastic stiffness of the ice-rock system depends on the temperature, and is unlikely to be explained by changes in the elastic properties of ice. Load point velocity oscillations induce oscillations in applied shear stress. Many natural fault systems exhibit slip behaviors that depend on harmonic oscillations in applied tidal stresses. Our new method provides a way to study how frictional properties directly depend on parameters relevant to tidal forcing, and how oscillatory loading must be considered when extracting friction parameters.

Oscillatory loading can alter the velocity rate dependence of ice-on-rock friction

Rob M. Skarbek[1], Christine McCarthy[1], Heather M. Savage[2]

[1]Lamont-Doherty Earth Observatory, Columbia University
[2]University of California, Santa Cruz

Key Points:

- We obtain rate and state parameter values directly from fits to load point velocity oscillation events.
- Oscillation events show dominantly velocity-weakening behavior, whereas velocity steps from the same experiments are velocity-strengthening.
- Elastic stiffness depends on the temperature in a way that is not explained by changes in the elastic properties of ice.

Corresponding author: Rob M. Skarbek, `rskarbek@ldeo.columbia.edu`

Abstract

Rate and state frictional parameters are typically determined using two types of experimental protocols: velocity steps and slide-hold-slide events. Here we take a new approach by examining the frictional response to controlled, harmonic oscillations in load point velocity. We present a Matlab graphical user interface software package, called RSFitOSC, that allows users to easily determine frictional parameters by fitting oscillation events using the rate and state friction equations. We apply our new methods to a set of ice-rock friction experiments conducted over a temperature range of $-16.4°$C to $-2°$C, and described in a companion paper: McCarthy et al. (In Review). Values of the frictional stability parameter $(a-b)$ determined from oscillations reveal dominantly velocity-weakening behavior across the entire range of experimental conditions. However, values of $(a-b)$ determined from velocity steps in the same experiments yield velocity-strengthening behavior. We also show that the elastic stiffness of the ice-rock system depends on the temperature, and is unlikely to be explained by changes in the elastic properties of ice. Load point velocity oscillations induce oscillations in applied shear stress. Many natural fault systems exhibit slip behaviors that depend on harmonic oscillations in applied tidal stresses. Our new method provides a way to study how frictional properties directly depend on parameters relevant to tidal forcing, and how oscillatory loading must be considered when extracting friction parameters.

Plain Language Summary

Tidal stresses are known to affect how faults slip on Earth and on other planets and moons, as well as the movements of landslides, glaciers, and ice sheets. Friction also plays an important role in governing these processes. In this paper, we develop a new technique for determining frictional properties from experiments in which the movement of samples are driven by an oscillating load that mimics a tidal signal. We apply our new method to a dataset of ice-rock experiments, and find that the frictional behavior can be different from what is found using traditional techniques for examining frictional properties.

1 Introduction

Tidal stress modulations occur in many geologic systems where friction plays an important role, including: the behavior of slow slip and non-volcanic tremor in subduction zones (Rubinstein et al., 2008) and along the San Andreas fault (Thomas et al., 2009; van der Elst et al., 2016); triggering of earthquakes along faults (Cochran et al., 2004; Scholz et al., 2019) and laboratory stick slip (Savage & Marone, 2007); movements on faults in icy satellites (Nimmo et al., 2007; Smith-Konter & Pappalardo, 2008; Spencer & Nimmo, 2013); movements of alpine glaciers (Kulessa et al., 2003); and landslides (Schulz et al., 2009). Often these observations are explained in terms of rate and state friction theory. In a companion to this paper, McCarthy et al. (In Review) describe ice-granite experiments in which we examine the frictional response to harmonic oscillations in the load point velocity, motivated by observations of modulation by tidal stresses in the movements of ice streams in Antarctica (Anandakrishnan & Alley, 1997; Anandakrishnan et al., 2003; Minchew et al., 2017). We found that imposed loading oscillations results in a wide range of sliding response, from steady sliding, to slow slip, to stick slip.

To better understand the data set and behaviors observed by McCarthy et al. (In Review), and to provide tools for understanding other types of tidally influenced slip behavior, we have developed a numerical inversion scheme that determines rate and state frictional parameters directly from the frictional response to load point oscillations. The scheme is applied using a graphical user interface (GUI) software package that is written in Matlab. Called RSFitOSC, the package is based on RSFit3000, a similar program

Exp No.	σ_n (kPa)	v_m (μm/s)	v_a (μm/s)	ω (Hz)
C29, C30, C32	100	10	2, 5, 10	0.01, 0.1, 1
C31, C33	100	10	2, 5, 10	0.01, 0.02, 0.1, 0.2, 1
C34, C39, C40	100	1, 10	5, 10	0.01, 0.1
C41, C44	500, 1000	1, 10	5, 10	0.01, 0.1

Table 1. Nominal parameter values used to define the experimental protocols from McCarthy et al. (In Review).

that was developed for analyzing velocity step and slide-hold-slide (SHS) events (Skarbek & Savage, 2019). RSFitOSC is available at `https://github.com/rmskarbek/RSFitOSC`.

Here we describe our inversion scheme and use RSFitOSC to apply our methods to the experiments conducted by McCarthy et al. (In Review). Our analysis of the oscillation events reveals that frictional stability depends on normal stress σ_n, and at low values of σ_n is velocity-weakening across the entire temperature range. This is in contrast to velocity step events from the same experiments that show velocity-strengthening stability behavior. The stability behavior of the ice-rock frictional system depends on the forcing characteristics induced by the load point movement. Oscillation events combine aspects of both velocity steps and SHS events, and it is possible that this may result in more unstable behavior. Finally, we suggest that oscillation events can be combined with velocity step and SHS events in experimental protocols, to enable more detailed studies of frictional behavior.

2 Summary of Experiments from McCarthy et al. 2020

McCarthy et al. (In Review) performed a series of ice-granite friction experiments in a double-direct shear configuration using a cryogenically cooled, servo-controlled biaxial shear apparatus (McCarthy et al., 2016). In these experiments a periodic signal with frequency ω was applied to the load point velocity v_l, so that at time t the velocity is

$$v_l = v_m + v_a \cos(2\pi\omega t) , \tag{1}$$

where v_m is the median driving velocity of the load point, and v_a is the half-amplitude of the signal. Each experimental run was conducted at a constant temperature in the range $-16.4°\text{C} \leq T \leq -2°\text{C}$, and the load point oscillations took place at a constant normal stress of 100 kPa, 500 kPa, or 1 MPa, and consisted of applying a succession of different signals (Table 1; for details, see McCarthy et al., In Review). In general, the load point signal resulted in a periodic frictional response with the same frequency as the load point. For the purposes of conducting parameter fits, we define oscillation events by the prevailing forcing parameters, as well as a window of time $t_i - t_f$ over which we applied a fit, where t_i may be up to a few cycles after a unique oscillation signal is applied.

Different protocols for controlling the load point velocity were implemented. Three experiments (C29, C30, C32) consisted of nine separate oscillation events each, defined by values of $v_m = 10$ μm/s; $v_a = 2$, 5, 10 μm/s; and $\omega = 0.01$, 0.1, 1 Hz. This protocol was also used for experiments C31 and C33, with additional frequencies $\omega = 0.02$, 0.2 Hz. Three experiments (C34, C39, C40) consisted of eight oscillations events each, defined by values of $v_m = 1$, 10 μm/s; $v_a = 5$, 10 μm/s; and $\omega = 0.01$, 0.1 Hz. Finally, two experiments (C41, C44) consisted of sixteen oscillation events defined by the same protocol as C34 for example, but at normal stresses $\sigma_n = 0.5$, 1 MPa. All of the experiments except for C29 – C33 contained a velocity step from 1 μm/s to 10 μm/s that

McCarthy et al. (In Review) used to determined rate and state frictional parameters. The total data set is comprised of one-hundred and thirteen unique oscillation events, as defined by the values of v_m, v_a, ω, σ_n, and T. Eighty-one events were conducted at 100 kPa normal stress, and sixteen each conducted at 0.5 and 1 MPa normal stress.

McCarthy et al. (In Review) observed a wide range of slip behaviors, including creep, slow slip, and stick slip events. Particularly they observed an evolution towards unstable behavior at higher normal stress. Their results did not reveal any temperature effects on the sliding behavior, except in the higher normal stress experiments. The primary effect of temperature is on the mean friction coefficient, which increases as temperature decreases, consistent with previous studies (Zoet et al., 2013; McCarthy et al., 2017). At elevated normal stress, more unstable behavior was observed at $-5°$C (C41) than at $-2°$C (C44); however since only two temperatures were examined, a relationship between temperature and stability behavior could not be confirmed. For each oscillation event, McCarthy et al. (In Review) measured the mid-to-peak $\mu_{\mathrm{m/p}}$ amplitude of the frictional response and showed that when $v_m = v_a$, the relationship between $\mu_{\mathrm{m/p}}$ and the oscillation period $1/\omega$ is consistent with frictional strengthening determined from slide-hold-slide experiments in a previous study on the same materials (McCarthy et al., 2017). Finally, the values of $(a-b)$ from the velocity steps are all velocity-strengthening, which is at odds with the clear observation of unstable behavior in some of these experiments.

3 Methods

Experimental friction measurements are typically made using two types of imposed friction events: velocity steps, and slide-hold-slide (SHS) events. In a velocity step, the load point is set in motion at a constant rate v_i for a sufficient displacement that a steady friction coefficient μ is achieved. The sliding rate of the load point is then changed as quickly as possible to a new value v_f, and maintained until μ achieves a new, steady value. A SHS event also initiates at a steady of μ at a load-point velocity v_{load}. The load point is stopped altogether for some amount of time t_{hold} (the hold), and then started moving again at a value v_{reload}, not necessarily equal to v_{load}.

The rate and state framework describes the friction coefficient μ on a sliding surface as a function of the sliding rate v and an internal state variable θ, such that

$$\mu = \mu_0 + a \ln\left(\frac{v}{v_0}\right) + b \ln\left(\frac{v_0\theta}{d_c}\right), \tag{2}$$

where a and b are frictional parameters; d_c is a length related to the amount of slip needed to attain a steady state after changes in sliding velocity; and μ_0 is a reference coefficient such that $\mu = \mu_0$ for steady sliding at v_0 (Dieterich, 1979; Ruina, 1983; Marone, 1998). This framework is completed by a description of how the state variable evolves, and here we will employ the slip law

$$\frac{\partial\theta}{\partial t} = -\frac{v\theta}{d_c}\ln\left(\frac{v\theta}{d_c}\right), \tag{3}$$

because it has been shown to be more consistent with experimental data than alternatives such as the aging law (Bhattacharya et al., 2015, 2017; Ferdowsi & Rubin, 2020). Applying the rate and state equations to experimental data requires a description of elasticity, and this is accomplished by assuming that the elastic response of the experimental apparatus (including the sample) can be adequately described by Hooke's law applied to a single-degree-of-freedom spring slider. In terms of velocity and the friction coefficient, the relation is

$$\frac{\partial\mu}{\partial t} = k(v_l - v), \tag{4}$$

where k is the elastic stiffness normalized by normal stress.

The frictional parameters are usually determined by applying equations (2) - (4) to velocity step events (e.g., Reinen & Weeks, 1993; Noda & Shimamoto, 2009; Skarbek & Savage, 2019). Our new method consists of applying an optimization routine of the spring-slider system to experimental data where the load point velocity is controlled by equation (1). RSFitOSC uses the same optimization techniques as RSFit3000, which are described in detail in Skarbek and Savage (2019). The program accomplishes fits to experimental data through a nonlinear least-squares optimization using the Levenberg-Marquardt method. The routine is started by providing trial values for the optimization parameters, here μ_0, a, b, d_c, and k. Then the best fit values of these parameters are found through an iterative process that involves simulating the spring-slider system and comparing the computed values of μ with the experimentally observed values. When the fitting routine completes, it computes errors to the optimized parameters values as twice the standard deviation in each value. As a measure of the "goodness" of a fit, the program computes the coefficient of determination R^2, where $R^2 = 1$ would indicate a perfect match between the experimental data and a numerical simulation that uses the optimized parameters.

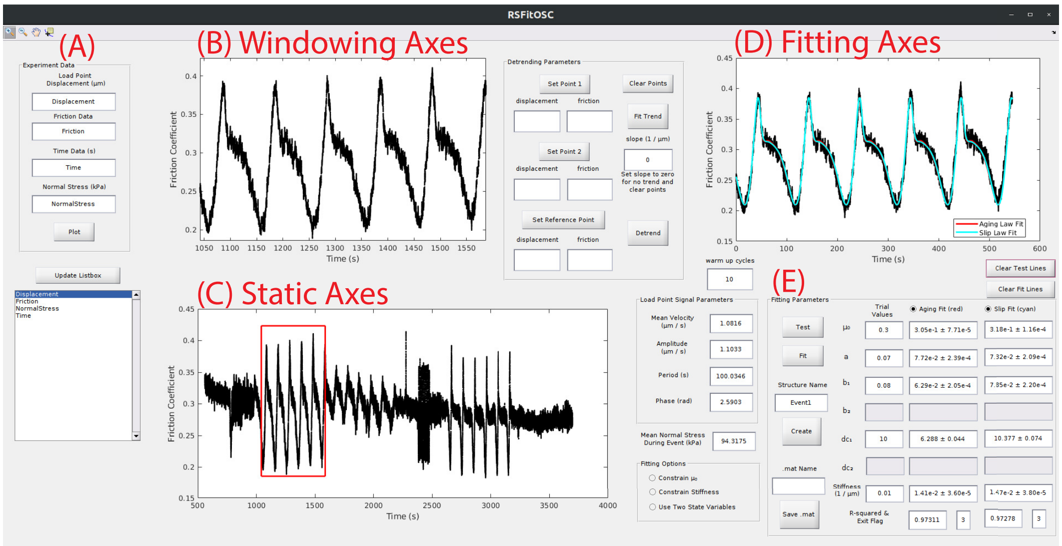

Figure 1. The RSFitOSC interface is composed of five main parts: (A) the Experimental Data Panel; (B) the Windowing Axes; (C) the Static Axes; (D) the Fitting Axes; and (E) the Fitting Parameters Panel. The entire interface is described in detail in the user manual, found at `https://github.com/rmskarbek/RSFitOSC`.

A key difference between fitting an oscillation event and fitting a velocity step event, is that oscillation events do not initiate from a steady state. Ideally, a velocity step is applied when the friction coefficient is not changing, so that the system is at steady-state. This provides the initial conditions $v(t_i) = v_i$, $\theta(t_i) = d_c/v_i$ for fitting the data, where t_i is the time at the beginning of the event. When fitting oscillation events, we do not want to the optimization routine to be influenced by transient behavior associated with the initial conditions of the simulation. To deal with this issue, every time the optimization routine runs a spring-slider simulation it goes through a number of "warm up" cycles, then goes through as many additional cycles as necessary to fit the experimental data (Figure S1).

Figure 1 shows the RSFitOSC interface and an example of how a fit is performed. A detailed user guide can be found along with the software package at `https://github.com/rmskarbek/RSFitOSC`. The interface has five main parts (I) the data input panel;

(II) the windowing axes; (III) the static axes; (IV) the fitting axes; (V) parameter value display. The user loads experimental data into Matlab and enters the appropriate variable names in the Experimental Data Panel. The entire experiment is shown in the Static Axes and the user zooms in on an event of interest in the Windowing Axes. A red box appears on the Static Axes, showing the location of the windowed data, and the event is shown in the Fitting Axes, plotted against a time coordinate t' that is zeroed to the beginning of the windowed data such that $t' = t - t_i$, where the event window is defined by $t_i \leq t \leq t_f$.

For obtaining accurate fits, it is important to use the actual velocity of the load point, rather than the nominal input parameters that control the load point motion. For a load point velocity given by equation (1), the load point displacement is given by

$$\delta_l = v_m t + \left(\frac{v_a}{\omega'}\right)\left[\sin\left(\omega' t + \gamma\right) - \sin\left(\gamma\right)\right] \ , \tag{5}$$

where $\omega' = 2\pi\omega$ is the angular frequency. When an event is windowed, RSFitOSC fits equation (5) to the recorded displacement of the load point within the window. The phase γ is needed because the windowed data will not necessarily begin at the start of a cycle. The values of v_m, v_a, ω, and γ so determined are then used in the optimization routine; these values can also be changed manually. For ease of reading, throughout the text we refer to specific oscillation events using the nominal values of v_m, v_a, ω, rather than the values determined using equation (5); however in many cases these differ by as much as 10%.

Finally, for each oscillation event that we fit, we also characterized the frictional response by determining the average friction coefficient μ_m and average half amplitude μ_a of the windowed data. The average friction coefficient is simply the mean value of μ during the window, and we calculated μ_a as one half of the difference between the mean values of the extrema during the event.

4 Results

For an oscillation event to be suitable for analysis, it must produce an inharmonic response in the shear stress. Because of the non-linear form of the spring-slider system equations, different sets of parameters can generate an identical harmonic (i.e. sinusoidal) frictional response. Events that produce a harmonic response cannot be fitted with a unique set of parameters using equations (2) – (4). However, we emphasize that harmonic events still contain important information about the frictional behavior (McCarthy et al., In Review).

In the experiments from McCarthy et al. (In Review), there were thirty-four events, all with $\omega = 1$ Hz, that we did not attempt to fit because the response clearly followed the sine wave form of the load point signal, or was not periodic (e.g. see Figures 2A and 3A in McCarthy et al., In Review). We conducted fits on the remaining seventy-nine events. Not all of the fits are of good quality, and because we are using a new technique, we took a conservative approach to defining additional criteria for accepting or rejecting a fit. After applying these criteria, we accepted forty-one fits. In this section we first describe the differences in fit quality that we observe, as well as our acceptance criteria. We then present the fitted parameter values from the accepted events. Plots of all of the fits can be found in the Supplemental Information.

First, we rejected any events that have a clear slip-dependent trend, that we define as when each peak in the frictional response is successively smaller (or larger) than the preceding peak. We rejected eight events based on this criterion (C29_3, C29_4, C31_5, C33_9, C39_8, C40_4, C41_6, C44_11). Slip-dependent trends are not uncommon in velocity step events, and the usual practice is to remove the trend and conduct a fit to the detrended data. However, the majority of the oscillation events do not have a slip-dependent trend, so we reject those that do to maintain a conservative approach to accepting fits.

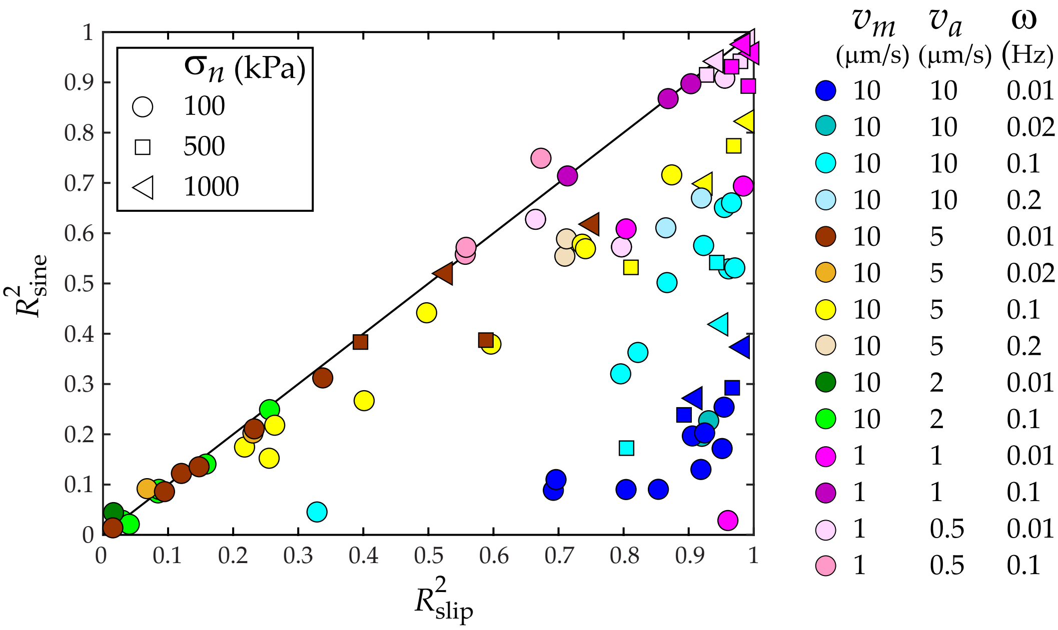

Figure 2. Values of R^2_{slip} and R^2_{sine} for all of the fits that we conducted, colored according to the load point signal parameters. Black line shows $R^2_{\text{slip}} = R^2_{\text{sine}}$.

As we noted, there are a number of events where the frictional response is well described by a sine wave, particularly when $v_m = 1$ μm/s. This observation prompted us to fit a sine wave of the form $\mu = \hat{\mu}_m + \hat{\mu}_a \sin(2\pi\omega t)$ to every event, where ω is the same frequency in the load point oscillation. The coefficients of determination R^2_{sine} for the sine wave fits are plotted against the corresponding values of R^2_{slip} from the slip law fits in Figure 2. When $R^2_{\text{sine}} \approx 1$, the fitted parameters for the slip law can have very large error estimates, and are likely dependent on the trial parameters that are used to produce the fit.

Most of the $v_m = 1$ μm/s events fall close to a line defined by $R^2_{\text{sine}} = R^2_{\text{slip}}$. All of the slip law fits for events with $v_m = 1$ μm/s, $\omega = 0.1$ Hz are indistinguishable from the corresponding sine wave fits (see Figure 3A for an example), regardless of the value of v_a, so these events are rejected. For the remaining $v_m = 1$ μm/s events, we conducted multiple slip law fits, each with a significantly different set of trail parameters. We rejected any events if the optimized parameter values depended on the trial values (C34_2, C34_4, C41_8, C44_7, C44_8). Applying this procedure, we accepted five events with $v_m = 1$ μm/s, $v_a = 1$ μm/s, $\omega = 0.01$ Hz (C39_3, C40_3, C41_1, C41_7, C44_1), and three events with $v_m = 1$ μm/s, $v_a = 0.5$ μm/s, $\omega = 0.01$ Hz (C39_4, C41_2, C44_2). Some of the accepted events have values $R^2_{\text{slip}} > R^2_{\text{sine}} > 0.9$, and so are well fit by a sine wave (e.g. Figure 3B), but not as well as the slip law. However, in these cases the phase of the simulated frictional response is sensitive to the value of d_c, and this seems to cause the fit to not depend on the trial parameter values.

For events with $v_m = 10$ μm/s, we observe a general divide between fits that cluster near the $R^2_{\text{sine}} = R^2_{\text{slip}}$ line when $R^2_{\text{slip}} < 0.6$, and fits that fall well below this line otherwise. However, when $R^2_{\text{slip}} < 0.6$ and $R^2_{\text{sine}} \approx R^2_{\text{slip}}$, the slip law and sine wave fits are distinct, and so the value of R^2_{sine} does not serve as a good criterion for reject-

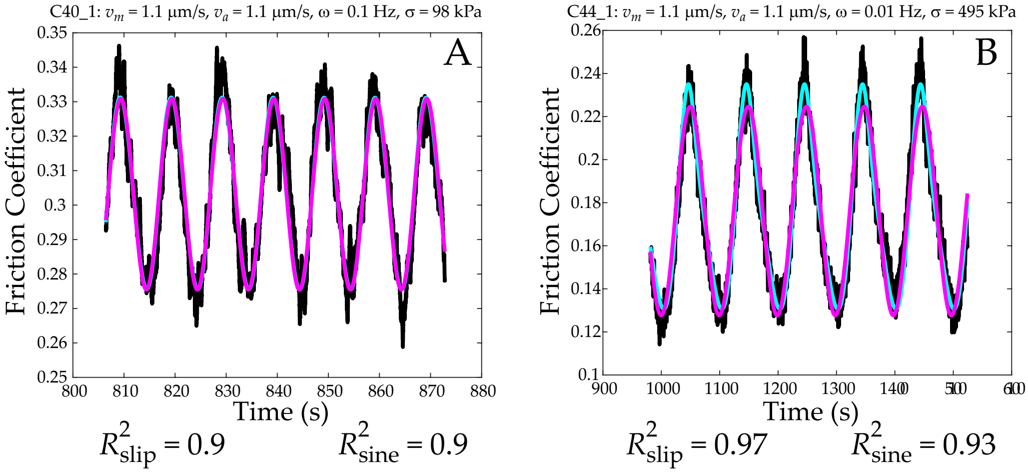

Figure 3. Examples of comparing slip law fits (cyan) with a sine wave fit (magenta); event parameters are displayed at the top of each panel. **(A)** A rejected event (C40_1) where the slip and sine wave fits are practically indistinguishable. The sine wave fit plots directly over the slip law fit. **(B)** An event (C44_1) with a high value of R^2_{sine} that was accepted because the slip law fit did not depend on the trial parameter values.

ing a fit. Instead we conservatively reject any fits with $R^2_{\text{slip}} < 0.7$. The highest R^2_{slip} values occur for events with $v_m = 10$ μm/s, $v_a = 10$ μm/s; all of these events have $R^2_{\text{slip}} > 0.7$ and so are accepted. Two events with $v_m = 10$ μm/s, $v_a = 10$ μm/s, and $\omega = 0.01$ Hz have $R^2_{\text{slip}} \approx 0.69$; these are accepted as well.

Finally, we accepted nine events with $v_m = 10$ μm/s and $v_a = 5$ μm/s. In total, we accepted eight events with $v_m = 1$ μm/s and thirty-three events with $v_m = 10$ μm/s. Of these fits, there are nine with $\sigma_n = 500$ kPa, five with $\sigma_n = 1$ MPa, and the remainder are $\sigma_n = 100$ kPa. Experimental and fitted parameters are shown in Table 2. Representative events that were accepted are shown in Figure 4, and representative rejected fits are shown in Figure 5. Accepted events are characterized by a well-defined inharmonic frictional response with clear extrema. Fits that were rejected based on the $R^2_{\text{slip}} < 0.7$ criterion are characterized by large amounts of noise in the frictional response. Although fits to these events give unique sets of frictional parameters, they are rejected because of the large mismatch between the simulated and observed responses (i.e. the value of R^2_{slip}).

4.1 Friction Parameters

Each fit produces a value of μ_0, a, b, d_c, and k according to equations (2) – (4). The experimental conditions are defined by five independent parameters: mean load point velocity v_m, load point signal amplitude v_a, load point signal frequency ω, normal stress σ_n, and temperature T. We have found that the clearest presentation of the fitting results is found by plotting against temperature (Figure 6B, 6D, 6F), and against the normalized frictional response amplitude $\mu'_a = \mu_a/\mu_m$ (Figure 6A, 6C, 6E).

Although μ'_a is not one of the independent control parameters, plots of the fitted parameters against μ'_a reveal a correlation with the normalized load point velocity amplitude $v'_a = v_a/v_m$, as well as with μ'_a. For $v_m = 10$ μm/s the fitted parameters fall into two distinct groups according to the value of v'_a. For $v'_a = 0.5$, $0.05 < \mu'_a < 0.16$; and for $v'_a = 1$, $0.2 < \mu'_a < 0.51$ (Figure 6A, 6C, 6E). No distinct separation is observed for $v_m = 1$ μm/s, but the smallest values of μ'_a occur for $v'_a = 0.5$, and the largest

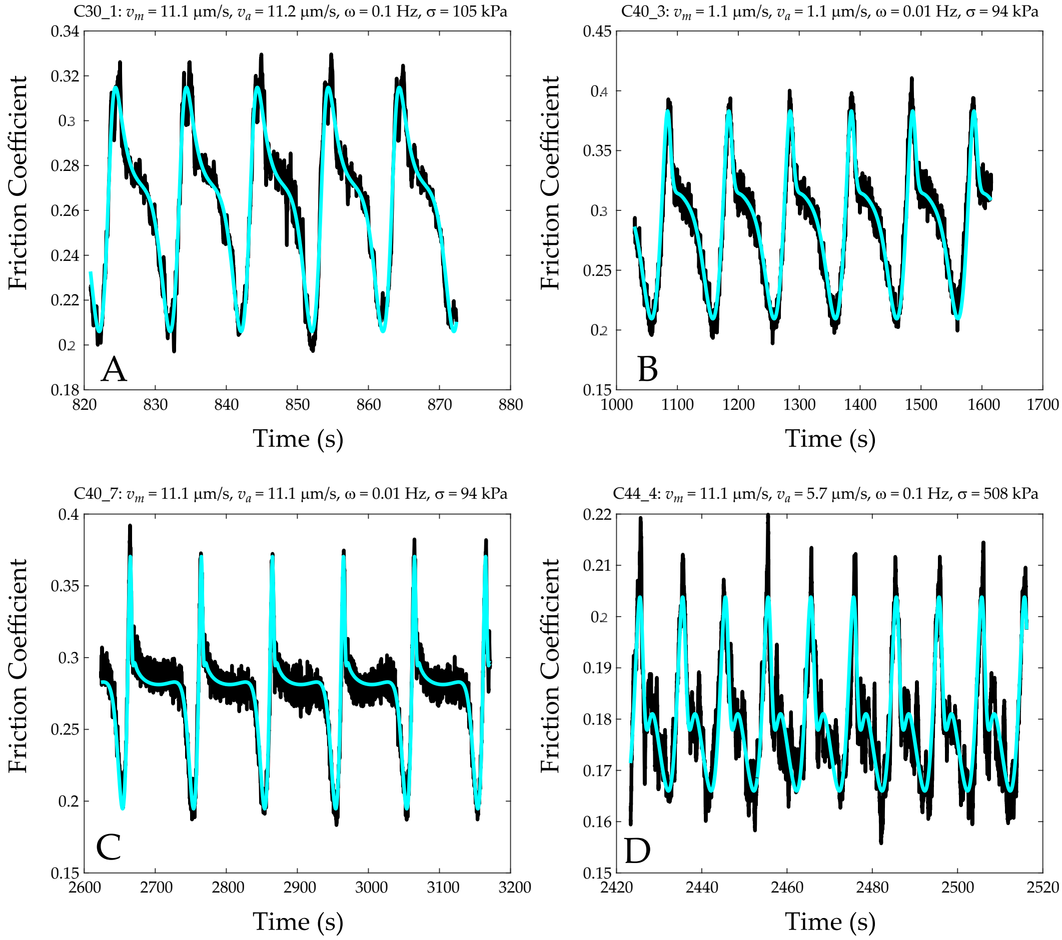

Figure 4. Examples of accepted fits for different types of load point signals. Event parameters are displayed at the top of each panel.

occur for $v'_a = 1$. We only accepted eight events with $v_m = 1$ μm/s, so it is possible that some type of correlation with μ'_a might exist if there were more events.

Since frictional stability depends on the value of $(a-b)$, we focus on this parameter rather than on a and b individually. The entire $(a-b)$ data set falls within the range $-0.02 < (a-b) < 0.01$ and most of the values are velocity-weakening. Every event with $\sigma_n = 100$ kPa has a best-fit value of $(a-b)$ that is less than zero, although two events (C39_6, C40_6) with $v_m = 10$ μm/s, $v_a = 5$ μm/s, and $\omega = 0.1$ Hz encompass $(a-b) > 0$ within their error-bars. Of the fourteen higher normal stress events, nine of them are velocity-strengthening. For $v_m = 10$ μm/s, values of $(a-b)$ are larger for $v'_a = 0.5$ than for $v'_a = 1$ and there is a general decrease in the value of $(a-b)$ with increasing μ'_a (Figure 6A). These observations loosely describe values of $(a-b)$ for $v_m = 1$ μm/s as well. There is no observed correlation between $(a-b)$ and temperature (Figure 6B). The slightly larger values at warmer temperatures are actually due to the values of v_a and σ_n, since experiments with $v_a = 5$ μm/s and higher normal stress were not conducted at colder temperatures (Table 1).

We also observe a correlation between the values of d_c and μ'_a (Figure 6C). For $v_m = 10$ μm/s, values of d_c fall within a smaller range ($5 < d_c < 10$ μm) for $v'_a = 0.5$ than for $v'_a = 1$ ($3 < d_c < 25$ μm). For events with $v_m = 1$ μm/s, there is no obvious distinction between events with $v_a = 0.5$ μm/s and those with $v_a = 1$ μm/s. For events

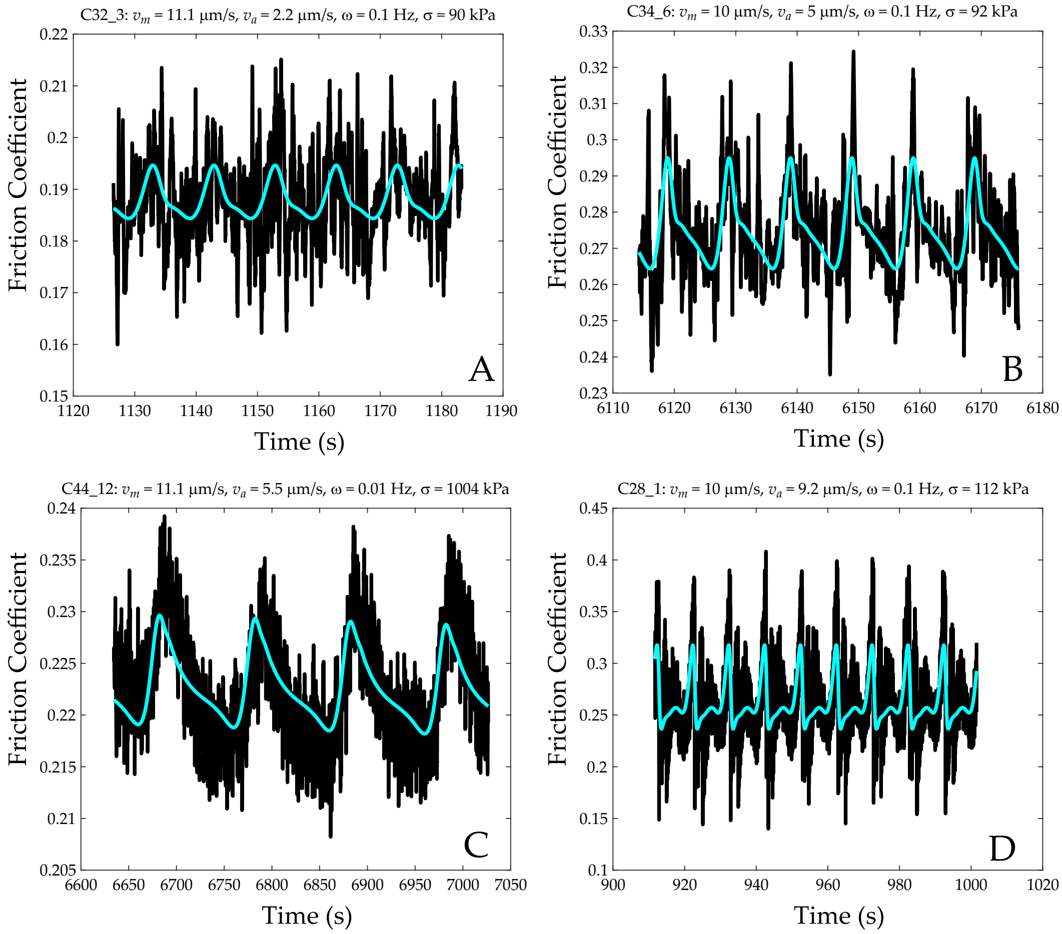

Figure 5. Examples of rejected fits for different types of load point signals. Event parameters are displayed at the top of each panel.

with $v_m = 1$ μm/s, aside from two events (C39_3, C44_1) with $d_c > 30$ μm, values of d_c are $10 < d_c < 23$ μm. Within the entire data set, there does not appear to be any correlation between d_c and normal stress. Possibly there is a correlation between d_c and the temperature when $v_m = 1$ μm/s, although there are not enough events in this category to confirm this (Figure 6D).

The stiffness values also correlate with the value of μ'_a, and fall into two groups according to the value of $v'_a = v_a/v_m$ (Figure 6E). For each value of v'_a (0.5 and 1), the value of k decreases approximately linearly from about 3 kPa/μm to about 1 kPa/μm with about the same slope. So the stiffness values do not appear to depend on the mean load point velocity v_m or amplitude v_a, and the two trends imply some other controls at work. Indeed, the stiffness does clearly depend on the temperature and the normal stress (Figure 6F). Values of stiffness increase linearly as the temperature decreases, and are larger at the higher normal stress values. According to a linear fit to the data, the change in stiffness of the $\sigma_n = 100$ kPa experiments is about -0.097 kPa/(μm °C). Within the $\sigma_n = 100$ kPa events, values of k are generally smallest for $v'_a = 1$, $v_m = 10$ μm/s, and $\omega = 0.01$ Hz. Since the higher normal stress experiments were only conducted at two temperatures, the dependence of k on temperature is not very reliable; however linear fits to those data yield essentially identical values of about -0.24 kPa/(μm °C).

Event	Temp (°C)	σ_n (kPa)	v_m $\left(\frac{\mu\text{m}}{\text{s}}\right)$	v_a $\left(\frac{\mu\text{m}}{\text{s}}\right)$	ω (Hz)	μ_0	a	b	$(a-b)$	d_c (μm)	k $\left(\frac{\text{kPa}}{\mu\text{m}}\right)$	R^2
C29_1	-14.7	87	9.9	9.7	0.1	0.352	0.042	0.056	-0.013	6.83	2.72	0.82
C30_1	-10	105	11.1	11.2	0.1	0.288	0.036	0.056	-0.02	16.62	2.18	0.96
C30_4	-10	106	11.1	11	0.01	0.293	0.052	0.06	-0.008	15.75	1.57	0.91
C31_1	-6	92	11.1	10.9	0.1	0.26	0.061	0.069	-0.009	6.78	1.28	0.96
C31_4	-6	92	11.1	11.1	0.01	0.263	0.062	0.077	-0.015	16.1	1.12	0.92
C31_6	-6	94	11.1	11.2	0.2	0.293	0.055	0.064	-0.008	6.18	1.66	0.92
C31_7	-6	94	11.1	5.7	0.2	0.29	0.058	0.067	-0.009	5.97	1.55	0.71
C31_8	-6	93	11.1	11.1	0.02	0.29	0.07	0.084	-0.014	10.26	1.31	0.93
C32_1	-2	92	11.1	11	0.1	0.189	0.056	0.062	-0.006	7.54	1.1	0.92
C32_2	-2	91	11.1	5.5	0.1	0.187	0.063	0.064	-0.001	6.48	1.03	0.74
C32_4	-2	87	11.1	11.1	0.01	0.191	0.064	0.077	-0.012	16.19	0.89	0.93
C33_1	-16.4	94	11.1	11.1	0.1	0.343	0.043	0.056	-0.014	9.3	2.22	0.87
C33_4	-16.4	95	11.1	11.1	0.01	0.325	0.063	0.069	-0.006	5.03	1.84	0.80
C33_6	-16.4	96	11.1	11.1	0.2	0.35	0.038	0.067	-0.029	11.46	2.23	0.87
C33_7	-16.4	96	11.1	5.7	0.2	0.341	0.048	0.054	-0.006	6.54	2.97	0.71
C33_8	-16.4	96	11.1	11	0.02	0.349	0.055	0.068	-0.013	10	2.18	0.92
C34_5	-5	92	10	10.2	0.1	0.273	0.061	0.067	-0.006	4.41	1.22	0.80
C34_7	-5	93	10	10.1	0.01	0.282	0.062	0.078	-0.015	13.93	0.92	0.85
C39_3	-2	101	1.1	1.1	0.01	0.178	0.051	0.084	-0.034	33.47	0.78	0.98
C39_4	-2	101	1.1	0.6	0.01	0.16	0.061	0.065	-0.004	23.12	0.66	0.96
C39_5	-2	102	11.1	11.1	0.1	0.157	0.038	0.049	-0.011	10.9	1.3	0.97
C39_6	-2	102	11.1	5.6	0.1	0.151	0.048	0.048	0	8.06	1.05	0.87
C39_7	-2	102	11.1	11.1	0.01	0.152	0.042	0.052	-0.01	18.84	0.87	0.95
C40_3	-10.7	94	1.1	1.1	0.01	0.317	0.073	0.078	-0.005	10.53	1.47	0.96
C40_5	-10.7	94	11	11	0.1	0.291	0.06	0.067	-0.007	5.73	1.76	0.97
C40_6	-10.7	93	11.1	5.6	0.1	0.291	0.058	0.059	0	5.39	1.67	0.74
C40_7	-10.7	94	11.1	11.1	0.01	0.286	0.068	0.076	-0.007	8.82	1.47	0.95
C41_1	-5	491	1.1	-1.1	0.01	0.258	0.072	0.056	0.016	11.56	2.16	0.99
C41_2	-5	492	1.1	0.5	0.01	0.255	0.072	0.055	0.017	12.76	2.4	0.98
C41_4	-5	490	11.1	5.6	0.1	0.266	0.044	0.043	0.001	10.63	3.07	0.97
C41_5	-5	490	11.1	11.1	0.01	0.277	0.049	0.056	-0.007	25.67	2.58	0.97
C41_7	-5	991	1.1	1.1	0.01	0.282	0.069	0.051	0.018	13.66	2.89	1.00
C41_9	-5	988	11.1	5.6	0.1	0.306	0.077	0.068	0.008	5.86	2.86	0.99
C41_10	-5	986	11.1	11.1	0.01	0.309	0.055	0.059	-0.004	23.75	3.27	0.98
C44_1	-2	495	1.1	1.1	0.01	0.209	0.046	0.08	-0.034	43.92	1.59	0.97
C44_2	-2	490	1.1	0.5	0.01	0.192	0.066	0.06	0.007	17.37	1.41	0.93
C44_3	-2	500	11	11.2	0.1	0.18	0.07	0.066	0.004	3.02	2.06	0.94
C44_4	-2	508	11.1	5.7	0.1	0.182	0.057	0.055	0.003	5.78	2.3	0.81
C44_5	-2	488	11.1	11.1	0.01	0.178	0.052	0.058	-0.005	15.45	1.8	0.89
C44_9	-2	998	11.1	11.1	0.1	0.189	0.068	0.066	0.002	2.98	2.2	0.95
C44_10	-2	994	11.1	5.6	0.1	0.196	0.053	0.051	0.002	6.83	2.39	0.95

Table 2. Load point signal and fitted parameters for accepted fits. Signal values are these determined using equation (5). Errors reported as two standard deviations can be found in Supplemental Information.

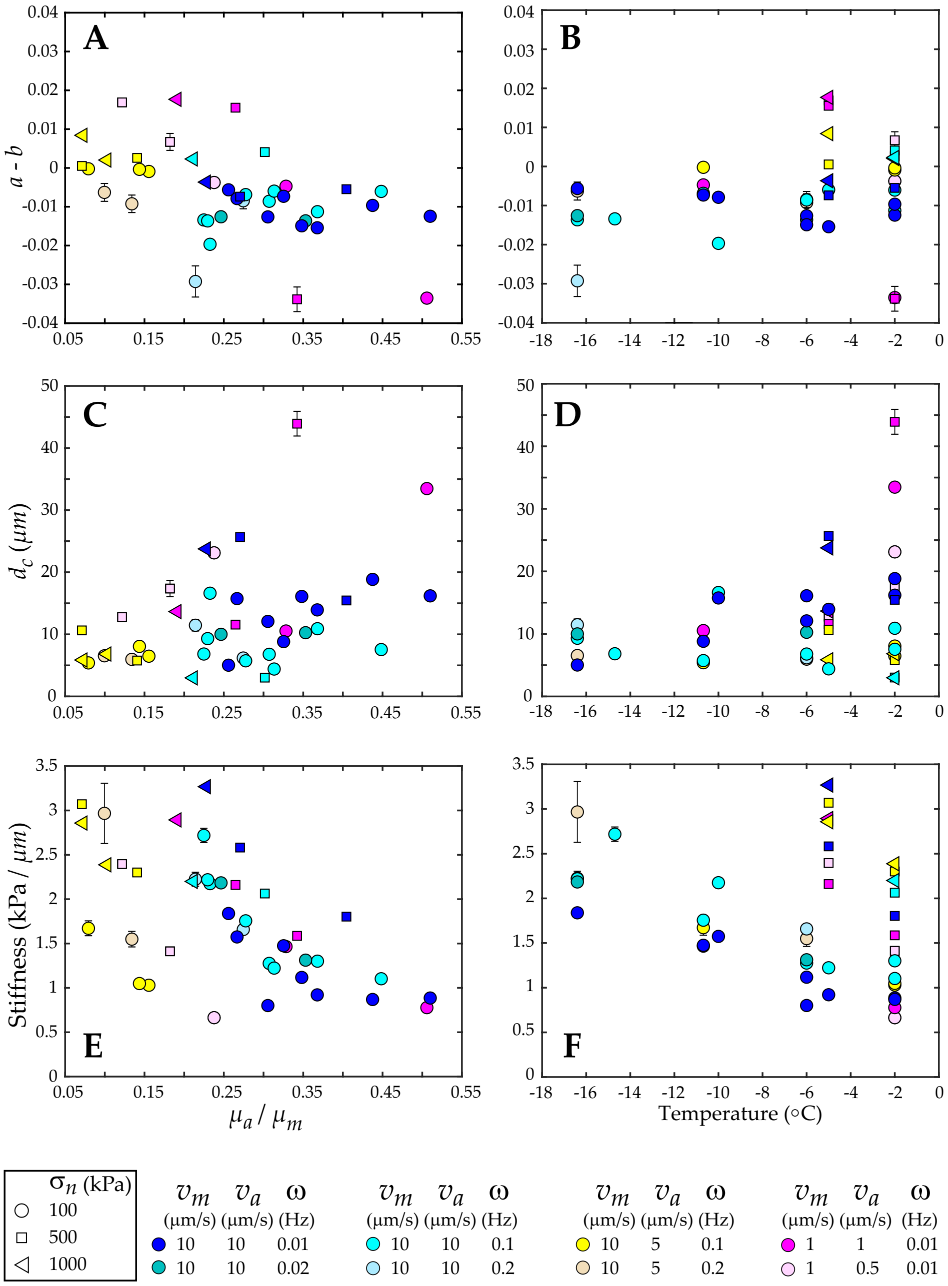

Figure 6. Values of $(a-b)$, d_c, and k for all of the accepted fits (Table 2); plotted against **(A, C, E)** the normalized frictional response amplitude; and **(B, D, F)** temperature.

5 Discussion

5.1 Stability Properties

Our observations of $(a-b)$ values from load point oscillation events provide the first evidence for velocity-weakening behavior in ice-rock friction at temperatures approaching the pressure melting point (PMP). However, experiments of ice-gouge friction have shown that velocity-weakening behavior can occur near the PMP, depending on gouge content and properties (Zoet et al., 2013, 2020). All of the fits to oscillations events with 100 kPa normal stress are velocity-weakening. Velocity-strengthening behavior appears

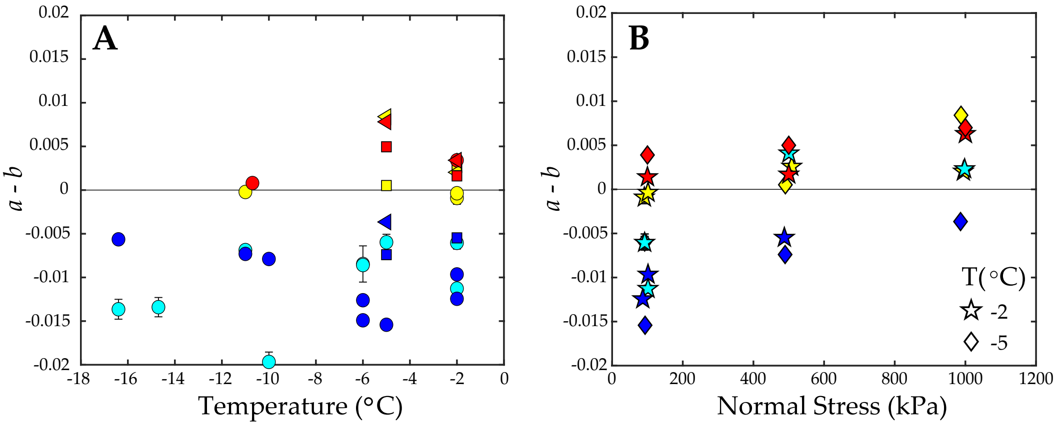

Figure 7. Dependence of $(a - b)$ values on **(A)** temperature and **(B)** normal stress. **(A)** Shows a subset of the data displayed in Figure 6B, to highlight similarities with values determined from velocity steps by McCarthy et al. (In Review) (red circles).

in 500 kPa and 1 MPa normal stress events, although data is only available for temperatures of $-2°$C and $-5°$C. We still observe velocity-weakening behavior at elevated normal stress for oscillations with $v_m = 10$ μm/s, $v_a = 10$ μm/s, and $\omega = 0.01$ Hz.

The velocity-weakening behavior exhibited by the oscillation events is in contrast to values of $(a-b)$ determined from fits to velocity steps in the same experiments (McCarthy et al., In Review). Experiments C34, C39, C40, C41, and C44 (conducted at temperatures of $-2°$C, $-5°$C, and $-10°$C, including those at higher normal stress) contained an up-step from 1 μm/s to 10 μm/s nominal load point velocity. Fits to these velocity steps all produce velocity-strengthening behavior (Figure 7A). The up-step $(a-b)$ values are broadly consistent with values determined from up-steps in a previous set of experiments on ice sliding against granite at $\sigma_n = 100$ kPa, conducted by McCarthy et al. (2017). They found that $(a - b)$ values transitioned from velocity-weakening at $T < -17°$C, to velocity-strengthening at higher temperatures. We also note that in a comparison of the up-step events with the oscillation events, the up-step $(a-b)$ values are most similar to values from oscillation events with $v_m = 10$ μm/s, $v_a = 5$ μm/s, and $\omega = 0.1$ Hz (yellow symbols in Figure 7A).

For both the oscillation and up-step fits there is a transition in the stability behavior as σ_n increases. The elevated normal stress experiments (C41, C44) both provide fits from a velocity step, and three unique oscillation signals. These can be compared to fits from $\sigma_n = 100$ kPa experiments C34 and C39, that also provide fits from velocity steps, and the same oscillation signals as in experiments C41 and C44 (Figure 7B). At low normal stress, only the up-steps are velocity-strengthening, and they provide values of $(a-b)$ that are similar in magnitude to those of the velocity-weakening oscillations with $v_m = 10$ μm/s, $v'_a = 0.5$, $\omega = 0.1$ Hz. As normal stress increases, more of the oscillation events are velocity-strengthening, and the minimum values of $(a-b)$ increase. So while we observe both velocity-weakening and -strengthening behavior in this subset of the data, the behavior becomes more velocity-strengthening as normal stress increases.

This type of behavior has not been observed before in ice-rock friction, or in ice-ice friction, since previous studies have focused on conducting experiments at a single normal stress (Zoet et al., 2013; McCarthy et al., 2017), or have not determined stability properties (Kennedy et al., 2000; Schulson & Fortt, 2012). There are some similar findings within the fault friction literature. For example, Saffer and Marone (2003) conducted friction experiments on smectite clay gouges and observed a transition from velocity-weakening to velocity-strengthening behavior as normal stress increased over about 30 MPa.

The subset of the data shown in Figure 7B also gives some indication of frequency-dependent stability behavior. We obtained fits to signals with $v_m = v_a = 10$ μm/s and four different values of ω in experiments conducted at -6°C (C31) and -16.4°C (C33). Both of these experiments show a consistent evolution of $(a-b)$ as ω changes (Figure 8). At -6°C the value of $(a - b)$ increases as ω increases, and at -16.4° the value of $(a-b)$ does the opposite. Although for experiments at other temperatures there are only two frequencies each with $v_m = v_a = 10$ μm/s, inspection of Figure 6B seems to support a transition in how the value of $(a-b)$ depends on ω at -10°C. For $T \leq -10$°C, $(a-b)$ is larger for $\omega = 0.01$ Hz, than for 0.1 Hz; the opposite is true for temperatures above -10°C. Clearly more data is needed to investigate this behavior.

Overall we have observed that the stability behavior of ice-rock friction depends on the normal stress and also on how the load point is moved (values of v_a' and ω), at least within the conditions defined by the experiments from McCarthy et al. (In Review). In these experiments, there is no temperature dependence in the stability behavior as determined from either the oscillation events or velocity steps. Models that include rate and state friction at the base of the ice, where temperatures are expected to be near the PMP, are a potential explanation for observations of stick-slip behavior at the Whillans Ice Plain in Antarctica (Lipovsky & Dunham, 2017). These models require values of $(a-b) < 0$ to reproduce observed behavior, so our results lend support to a frictional explanation for icy stick-slip behavior.

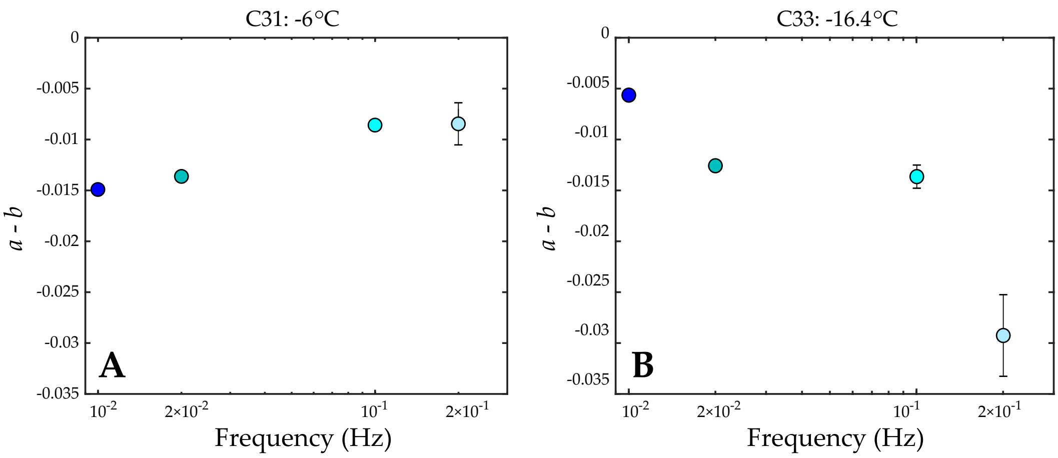

Figure 8. Frequency dependence of $(a-b)$ values for experiments conducted at **(B)** -6°C and **(B)** -16°C.

5.2 Relation of Oscillation Events to Velocity Steps and SHS Events and Implications for Rate-State Friction

There are some similarities between the oscillation events and velocity steps, or SHS events, depending on the characteristics of the load point signal. McCarthy et al. (In Review) showed that the frictional response amplitude μ_a from oscillation events with $v_m = v_a$ is of similar magnitude to the frictional strength measured from SHS events conducted on identical materials by McCarthy et al. (2017) (see Figure 4 in McCarthy et al., In Review). In this comparison, the period of an oscillation event is analogous to the hold time of a SHS event. Additionally, we have shown in Figure 7 that values of $(a-b)$ from oscillation events with $v_m = 2v_a$ are similar to $(a - b)$ values from velocity up-steps at the same temperature.

These observations suggest that in terms of frictional behavior, oscillation events may act as a type of transitional event between the two end members of velocity-step and SHS events. Velocity-steps are commonly used to determine stability behavior and values of frictional parameters. SHS events are generally used to study frictional healing, and can also be used to determine frictional parameter values (Marone & Saffer, 2015; Bhattacharya et al., 2017); however they are often not used in this manner. Oscillation events can combine elements of both velocity steps and SHS events, and so may serve as a method to examine the interplay between stability and healing behaviors in a single event type, or as a transition between the two other event types.

For example, as the value of v_a approaches that of v_m ($v'_a \to 1$), more healing can take place because the load point velocity begins to approach zero during the slowing down phase of the load point signal. The amount of time over which this occurs depends on the frequency of the load point signal, and so events with $v'_a \approx 1$ mimic those of a SHS event. McCarthy et al. (In Review) examined these similarities in detail. When $v_a < v_m$, less healing can take place and the oscillation event is more similar to a velocity step than a SHS event. The value of ω determines how fast the transition between the load point's maximum and minimum values occurs. For example, consider the signal with $v_m =$ 10 μm/s, $v_a = 5$ μm/s, and $\omega = 0.1$ Hz (events with $(a - b)$ values similar to those of velocity steps). Here v_l changes from 5 μm/s to 15 μm/s in 5 s, reaching a peak acceleration of $2\pi\omega v_a = 3.14$ μm/s^2. The velocity steps in the same experiments are from 1 to 10 μm/s, so the change in load point velocity is of similar magnitude, although a velocity step takes place more abruptly.

Finally, we want to highlight the importance of the implication that loading conditions can affect the rate-state parameters. Most natural systems experience oscillatory loading through the solid earth and ocean tides, as well as transient oscillations such as seismic waves. Our results suggest that when the oscillation amplitude is small compared to the driving velocity, velocity step experiments will accurately predict the rate-state parameters. However, when the oscillation amplitude is large, those values will be inaccurate. The friction rate dependence of the material is not strictly a material property, but a function of the loading conditions as well. This helps explain why unstable behavior is observed in places like the deep San Andreas fault (Thomas et al., 2009; van der Elst et al., 2016)), where tremor is modulated by earth tides. Although the depths suggest that the fault should be velocity strengthening, the oscillatory loading can drive those values towards velocity weakening through an increase in healing during the slowest part of the oscillation.

We propose that multiple loading conditions be considered during experiments to get a full sense of the rate dependence behavior of the material. This concept has also recently been explored by Ikari et al. (2020), who conducted "velocity cycle" tests. They implemented a SHS protocol, but instead of completely stopping the load point, they applied a small driving velocity. Their results showed, that the velocity cycle loading could induce changes in the stability properties, relative to those determined from velocity-step tests, similar to our observation that oscillatory loading can do the same.

5.3 Temperature Dependence

The elastic stiffness in equation (4) is the only fitting parameter in which we observe a clear temperature dependence (Figure 9A). Also, McCarthy et al. (2017) and McCarthy et al. (In Review) documented a well defined increase in frictional strength as temperatures decrease. Figure 9B shows their data, as well as our values of μ_m, the mean friction during an individual oscillation event. In this section we discuss possible connec-

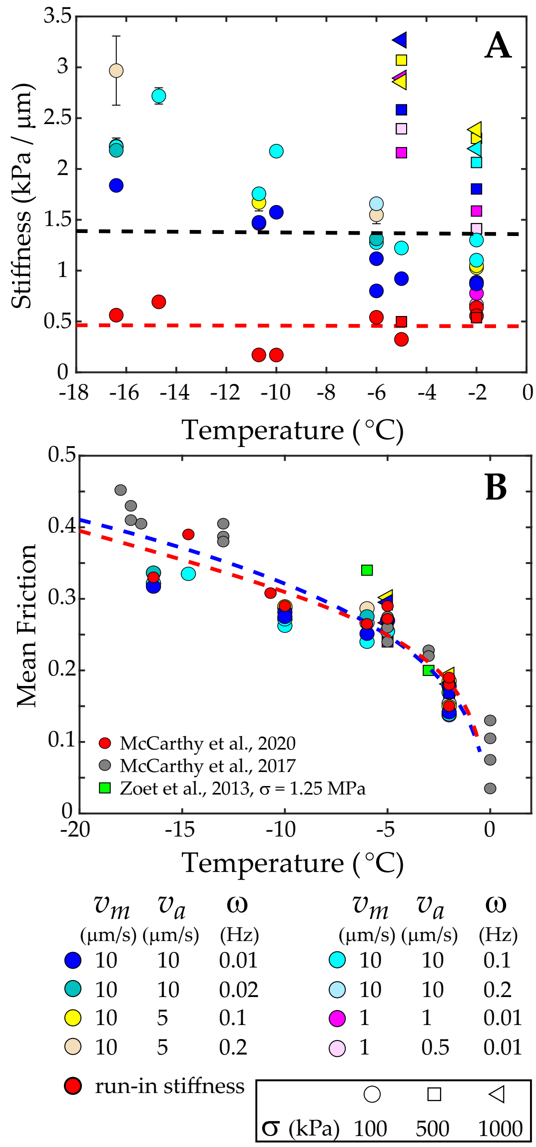

Figure 9. Temperature dependence of **(A)** elastic stiffness and **(B)** mean friction coefficient. **(A)** Dashed lines show predictions of the elastic full-space model using $\lambda = 5$ m (black) and $\lambda = 15$ m (red). Red circles show run-in stiffnesses determined by McCarthy et al. (In Review). **(B)** Dashed lines show predictions based on the models of Persson (2015) (blue) and Schulson (2015) (red). Additional data are from Zoet et al. (2013); McCarthy et al. (2017, In Review).

tions between elastic stiffness and frictional strength, and potential explanations for the temperature dependence in those parameters.

Figure 9A also shows stiffness values determined from the run-in portion of each experiment (see McCarthy et al., In Review, Table 1). The run-in is the beginning of an experiment, during which the load point is moved at a constant velocity and the shear stress increases approximately linearly from zero, as the sliding surface evolves to accommodate a steady-state value of the friction coefficient. Stiffness values are determined from the run-in by fitting a line to a plot of shear stress against load point displacement. The run-in stiffness values do not show any dependence on temperature, and are clustered around a value of 0.5 kPa/μm, such that at $-2°$C, these values correspond with the lower range of values determined from the oscillation events.

First, we make a basic estimate of how temperature-dependent changes in the elastic properties of ice might affect the stiffness values. Over the temperature range of the experiments from McCarthy et al. (In Review), the shear modulus G of ice increases from around 8.7 GPa at $-2°$C, to around 9 GPa at $-18°$C (Neumeier, 2018). Changes in ice shear modulus can be related to changes in elastic stiffness in a simple manner by considering slip on a planar fault embedded in a 2-D elastic full-space. For this system, along-fault changes in shear stress caused by gradients in slip s are given by (Segall, 2010)

$$\Delta\tau = \frac{G}{2\pi}\int_{\infty}^{\infty}\frac{\partial s/\partial\xi}{\xi - x}\mathrm{d}\xi\ , \tag{6}$$

where x is distance along the fault, and ξ is an integration variable that takes on all values of x. For a general sinusoidal slip distribution with wavelength λ, $s(x) = D\sin(2\pi x/\lambda)$, the change in shear stress is $\Delta\tau = (G/4\pi\lambda)s$. Then by analogy with equation (4), the stiffness of the full-space system is $k_{\mathrm{FS}} = G/4\pi\lambda$. To compare this with the experimental stiffness values, we can chose a value of the wavelength such that slip will not vary significantly over a distance equal to the length of the experimental sliding surface, 5 cm (McCarthy et al., In Review). The temperature dependence of k_{FS} is of primary interest, rather than its magnitude, since we can arbitrarily change the magnitude of k_{FS} by choosing different values of λ. Calculations for two values of λ are displayed in Figure 9A, the details of which can be found in the Supplemental Information.

We see that according to the analysis here, we should not expect temperature-dependent changes in elastic stiffness as a result of changes in the ice shear modulus. This analysis is however very approximate, in that we are comparing stiffness values determined from considering slip on a fault in an elastic full-space, to those determined from applying a spring-slider system to slip in an experimental bi-axial apparatus. Since the stiffness of a sliding surface in an elastic medium depends on geometrical features as well as the slip distribution, it is possible that an elastic model that incorporates a more accurate approximation of the geometrical features of a double direct shear apparatus may explain the temperature dependence that we observe. The single degree of freedom provided by the spring-slider model, although widespread and used for decades, may in fact be insufficient to capture important elastic effects that occur during bi-axial friction experiments.

It is possible that the change in stiffness observed in the oscillation events is due to the same processes that cause the mean friction coefficient to increase as temperatures become colder. The mean friction coefficient increases by about a factor of two, while the stiffness increases by about a factor 2.5. The similar rate of increase suggests that there may be some connection between the two parameters. The fact that the run-in stiffnesses are relatively constant, suggests that these values might reflect the stiffness of just the experimental apparatus. And a simple explanation for the temperature dependence of the oscillation stiffnesses is that they include effects due to the condition of the sliding surface, which depends on temperature as reflected in the mean friction coefficient μ_m. At warmer temperatures when μ_m is small, the sliding surface is less stiff, so the oscillation values fall closer to the run-in stiffness values.

Two recent papers provide some basic explanations for the temperature dependence of the friction coefficient in ice-ice sliding. Persson (2015) invoked "heat-softening" of the sliding surface; a process that progressively reduces the shear strength as the bulk melting temperature is approached, and made use of a phenomenological expression for the strength reduction that may be related to ice premelting. He developed this theory for ice-ice friction, but ice premelting also occurs at ice-rock interfaces (Rempel et al., 2001). A similar explanation comes from Schulson (2015). Schulson (2015) considered creep within an inelastic zone that encompasses the nominal sliding surface, and formulated the friction coefficient in terms of temperature dependent changes to the creep strength of this layer, combined with the same for the hardness of ice. Similar to Persson (2015), he also invoked localized melting at the sliding interface through a phenomenological expression (equation (43) in Schulson, 2015).

In Figure 9B we apply the theories from Schulson (2015) and Persson (2015), adapted for ice-granite friction (see the Supplemental Information for details). Each theory contains some unconstrained parameters that we have used to tune to the data. With that caveat in mind, both theories can provide reasonably good fits to the friction data. Although we are not aware of any theories directly relating the friction coefficient to the elastic stiffness of a sliding interface, based on the results here we suggest that such may be the case. Further work in this area is needed. It seems reasonable to hypothesize that whatever affects the friction coefficient may also affect the stiffness of the sliding interface.

6 Conclusion

Our results show that the stability behavior of ice-rock friction depends on the normal stress and also on loading conditions. Analysis of oscillation events indicates dominantly velocity-weakening behavior, whereas velocity-step events indicate velocity-strengthening. We attribute this difference to the presence of frictional healing in oscillation events. In general, our results suggest that when the oscillation amplitude is small compared to the driving velocity, velocity step experiments will accurately predict the rate-state parameters. However, when the oscillation amplitude is large, those values will be inaccurate. Finally, we observed a strong correlation between elastic stiffness and temperature, which cannot be explained by temperature-dependent changes in the elastic properties of ice. We presented a simple analysis that indicates a dependence of stiffness on the mean frictional strength.

Acknowledgments

We thank Rob Viesca for a helpful discussion on fault stiffness. All data generated for this study are available in the Supplemental Information. At time of acceptance, data will be archived on the United States Antarctic Program Data Center. The RSFitOSC software and user guide are available at `https://github.com/rmskarbek/RSFitOSC`.

References

Anandakrishnan, S., & Alley, R. B. (1997). Tidal forcing of basal seismicity of ice stream c, West Antarctica, observed far inland. *J. Geophys. Res.*, *102*(B7), 15183-15196. Retrieved from `https://agupubs.onlinelibrary.wiley.com/doi/abs/10.1029/97JB01073` doi: 10.1029/97JB01073

Anandakrishnan, S., Voigt, D. E., Alley, R. B., & King, M. A. (2003). Ice stream D flow speed is strongly modulated by the tide beneath the Ross Ice Shelf. *Geophys. Res. Lett.*, *30*(7). Retrieved from `https://agupubs.onlinelibrary.wiley.com/doi/abs/10.1029/2002GL016329` doi: 10.1029/2002GL016329

Bhattacharya, P., Rubin, A. M., Bayart, E., Savage, H. M., & Marone, C. (2015). Critical evaluation of state evolution laws in rate and state friction: Fitting large velocity steps in simulated fault gouge with time-, slip-, and stress-dependent constitutive laws. *J. Geophys. Res.*, *120*(9), 6365-6385. Retrieved from `https://agupubs.onlinelibrary.wiley.com/doi/abs/10.1002/2015JB012437` doi: 10.1002/2015JB012437

Bhattacharya, P., Rubin, A. M., & Beeler, N. M. (2017). Does fault strengthening in laboratory rock friction experiments really depend primarily upon time and not slip? *J. Geophys. Res.*, *122*(8), 6389-6430. Retrieved from `https://`

agupubs.onlinelibrary.wiley.com/doi/abs/10.1002/2017JB013936 doi: 10.1002/2017JB013936

Cochran, E. S., Vidale, J. E., & Tanaka, S. (2004). Earth tides can trigger shallow thrust fault earthquakes. *Science*, *306*(5699), 1164–1166. Retrieved from https://science.sciencemag.org/content/306/5699/1164 doi: 10.1126/science.1103961

Dieterich, J. H. (1979). Modeling of rock friction: 1. Experimental results and constitutive equations. *J. Geophys. Res.*, *84*(B5), 2161-2168. Retrieved from https://agupubs.onlinelibrary.wiley.com/doi/abs/10.1029/JB084iB05p02161 doi: 10.1029/JB084iB05p02161

Ferdowsi, B., & Rubin, A. M. (2020). A granular physics-based view of fault friction experiments. *J. Geophys. Res.*, *125*(6), e2019JB019016. Retrieved from https://agupubs.onlinelibrary.wiley.com/doi/abs/10.1029/2019JB019016 doi: 10.1029/2019JB019016

Ikari, M. J., Carpenter, B. M., Scuderi, M. M., Collettini, C., & Kopf, A. J. (2020). Frictional strengthening explored during non-steady state shearing: Implications for fault stability and slip event recurrence time. *J. Geophys. Res.*, *125*(10), e2020JB020015. Retrieved from https://agupubs.onlinelibrary.wiley.com/doi/abs/10.1029/2020JB020015 (e2020JB020015 2020JB020015) doi: https://doi.org/10.1029/2020JB020015

Kennedy, F. E., Schulson, E. M., & Jones, D. E. (2000). The friction of ice on ice at low sliding velocities. *Philos. Mag. A*, *80*(5), 1093-1110. Retrieved from https://doi.org/10.1080/01418610008212103 doi: 10.1080/01418610008212103

Kulessa, B., Hubbard, B., Brown, G. H., & Becker, J. (2003). Earth tide forcing of glacier drainage. *Geophys. Res. Lett.*, *30*(1), 11-1-11-4. Retrieved from https://agupubs.onlinelibrary.wiley.com/doi/abs/10.1029/2002GL015303 doi: https://doi.org/10.1029/2002GL015303

Lipovsky, B. P., & Dunham, E. M. (2017). Slow-slip events on the whillans ice plain, antarctica, described using rate-and-state friction as an ice stream sliding law. *J. Geophys. Res.*, *122*(4), 973-1003. Retrieved from https://agupubs.onlinelibrary.wiley.com/doi/abs/10.1002/2016JF004183 doi: https://doi.org/10.1002/2016JF004183

Marone, C. (1998). Laboratory-derived friction laws and their application to seismic faulting. *Annu. Rev. Earth Planet. Sci.*, *26*, 643–696. doi: 10.1146/annurev.earth.26.1.643

Marone, C., & Saffer, D. (2015). The mechanics of frictional healing and slip instability during the seismic cycle. In H. Kanimori (Ed.), *Treatise on geophysics* (2nd ed.). Oxford, U.K.: Elesvier.

McCarthy, C., Savage, H., & Nettles, M. (2017). Temperature dependence of ice-on-rock friction at realistic glacier conditions. *Phil. Trans. R. Soc. A*, *375*(2086), 20150348. doi: 10.1098/rsta.2015.0348

McCarthy, C., Savage, H. M., Koczynski, T., & Nielson, M. A. (2016). An apparatus to measure frictional, anelastic, and viscous behavior in ice at temperate and planetary conditions. *Review of Scientific Instruments*, *87*(5), 055112. Retrieved from https://doi.org/10.1063/1.4950782 doi: 10.1063/1.4950782

McCarthy, C., Skarbek, R. M., & Savage, H. M. (In Review). Tidal modulation of ice streams: Effect of periodic sliding velocity on ice friction and healing. *Frontiers in Earth Science*.

Minchew, B. M., Simons, M., Riel, B., & Milillo, P. (2017). Tidally induced variations in vertical and horizontal motion on Rutford Ice Stream, West Antarctica, inferred from remotely sensed observations. *J. Geophys. Res.*, *122*(1), 167-190. Retrieved from https://agupubs.onlinelibrary.wiley.com/doi/abs/10.1002/2016JF003971 doi: 10.1002/2016JF003971

Neumeier, J. J. (2018). Elastic constants, bulk modulus, and compressibility of

H2O ice Ih for the temperature range 50 K-273 K. *J. Phys. Chem. Ref. Data*, *47*(3), 033101. Retrieved from https://doi.org/10.1063/1.5030640 doi: 10.1063/1.5030640

Nimmo, F., Spencer, J., Pappalardo, R., & Mullen, M. (2007). Shear heating as the origin of the plumes and heat flux on Enceladus. *Nature*, *447*(7142), 289–291. doi: https://doi.org/10.1038/nature05783

Noda, H., & Shimamoto, T. (2009). Constitutive properties of clayey fault gouge from the hanaore fault zone, southwest japan. *J. Geophys. Res.*, *114*(B4). Retrieved from https://agupubs.onlinelibrary.wiley.com/doi/abs/10.1029/2008JB005683 doi: 10.1029/2008JB005683

Persson, B. N. J. (2015). Ice friction: Role of non-uniform frictional heating and ice premelting. *J. Chem. Phys.*, *143*(22), 224701. Retrieved from https://doi.org/10.1063/1.4936299 doi: 10.1063/1.4936299

Reinen, L. A., & Weeks, J. D. (1993). Determination of rock friction constitutive parameters using an iterative least squares inversion method. *J. Geophy. Res.*, *98*(B9), 15937-15950. Retrieved from https://agupubs.onlinelibrary.wiley.com/doi/abs/10.1029/93JB00780 doi: 10.1029/93JB00780

Rempel, A. W., Wettlaufer, J. S., & Worster, M. G. (2001, Aug). Interfacial premelting and the thermomolecular force: Thermodynamic buoyancy. *Phys. Rev. Lett.*, *87*, 088501. Retrieved from https://link.aps.org/doi/10.1103/PhysRevLett.87.088501 doi: 10.1103/PhysRevLett.87.088501

Rubinstein, J. L., La Rocca, M., Vidale, J. E., Creager, K. C., & Wech, A. G. (2008). Tidal modulation of nonvolcanic tremor. *Science*, *319*, 186–189. doi: 10.1126/science.1150558

Ruina, A. (1983). Slip instability and state variable friction laws. *J. Geophys. Res.*, *88*, 10,359-10,370.

Saffer, D. M., & Marone, C. (2003). Comparison of smectite- and illite-rich gouge frictional properties: Application to the updip limit of the seismogenic zone along subduction megathrusts. *Earth Planet. Sci. Lett.*, *215*(1-2), 219 - 235. Retrieved from http://www.sciencedirect.com/science/article/pii/S0012821X03004242 doi: http://dx.doi.org/10.1016/S0012-821X(03)00424-2

Savage, H. M., & Marone, C. (2007). Effects of shear velocity oscillations on stick-slip behavior in laboratory experiments. *J. Geophys. Res.*, *112*(B2). Retrieved from https://agupubs.onlinelibrary.wiley.com/doi/abs/10.1029/2005JB004238 doi: 10.1029/2005JB004238

Scholz, C. H., Tan, Y. J., & Albino, F. (2019). The mechanism of tidal triggering of earthquakes at mid-ocean ridges. *Nat. Commun.*, *10*(1), 1–7. doi: https://doi.org/10.1038/s41467-019-10605-2

Schulson, E. M. (2015). Low-speed friction and brittle compressive failure of ice: fundamental processes in ice mechanics. *International Materials Reviews*, *60*(8), 451-478. Retrieved from https://doi.org/10.1179/1743280415Y.0000000010 doi: 10.1179/1743280415Y.0000000010

Schulson, E. M., & Fortt, A. L. (2012). Friction of ice on ice. *J. Geophys. Res.*, *117*(B12). Retrieved from https://agupubs.onlinelibrary.wiley.com/doi/abs/10.1029/2012JB009219 doi: 10.1029/2012JB009219

Schulz, W. H., Kean, J. W., & Wang, G. (2009). Landslide movement in southwest Colorado triggered by atmospheric tides. *Nature Geosc.*, *2*(12), 863–866. doi: https://doi.org/10.1038/ngeo659

Segall, P. (2010). *Earthquake and volcano deformation.* Princeton, N.J.: Princeton Univ. Press.

Skarbek, R. M., & Savage, H. M. (2019). RSFit3000: A MATLAB GUI-based program for determining rate and state frictional parameters from experimental data. *Geosphere*, *15*(5), 1665-1676. Retrieved from https://doi.org/10.1130/GES02122.1 doi: 10.1130/GES02122.1

Smith-Konter, B., & Pappalardo, R. T. (2008). Tidally driven stress accumulation and shear failure of Enceladus's tiger stripes. *Icarus*, *198*(2), 435 - 451. Retrieved from http://www.sciencedirect.com/science/article/pii/S0019103508002704 doi: https://doi.org/10.1016/j.icarus.2008.07.005

Spencer, J. R., & Nimmo, F. (2013). Enceladus: An active ice world in the saturn system. *Annu. Rev. Earth Planet. Sci.*, *41*(1), 693-717. Retrieved from https://doi.org/10.1146/annurev-earth-050212-124025 doi: 10.1146/annurev-earth-050212-124025

Thomas, A. M., Nadeau, R. M., & Bürgmann, R. (2009). Tremor–tide correlations and near-lithostatic pore pressure on the deep San Andreas fault. *Nature*, *462*(7276), 1048–1051.

van der Elst, N. J., Delorey, A. A., Shelly, D. R., & Johnson, P. A. (2016). Fortnightly modulation of San Andreas tremor and low-frequency earthquakes. *Proc. Natl. Acad. Sci. U.S.A.*, *113*(31), 8601–8605. Retrieved from https://www.pnas.org/content/113/31/8601 doi: 10.1073/pnas.1524316113

Zoet, L. K., Carpenter, B., Scuderi, M., Alley, R. B., Anandakrishnan, S., Marone, C., & Jackson, M. (2013). The effects of entrained debris on the basal sliding stability of a glacier. *Journal of Geophysical Research: Earth Surface*, *118*(2), 656–666. Retrieved from http://dx.doi.org/10.1002/jgrf.20052 doi: 10.1002/jgrf.20052

Zoet, L. K., Ikari, M. J., Alley, R. B., Marone, C., Anandakrishnan, S., Carpenter, B. M., & Scuderi, M. M. (2020). Application of constitutive friction laws to glacier seismicity. *Geophysical Research Letters*, *47*(21), e2020GL088964. Retrieved from https://agupubs.onlinelibrary.wiley.com/doi/abs/10.1029/2020GL088964 (e2020GL088964 2020GL088964) doi: https://doi.org/10.1029/2020GL088964

Supporting Information for "Oscillatory loading can alter the velocity rate dependence of ice-on-rock friction"

Rob M. Skarbek[1], Christine McCarthy[1], Heather M. Savage[2]

[1]Lamont-Doherty Earth Observatory, Columbia University

[2]University of California, Santa Cruz

Contents of this file

1. Text S1
2. Figure S1

Additional Supporting Information (Files uploaded separately)

1. Captions for Datasets S1 to S13
2. Captions for large Tables S1 to S2

Introduction

This supplement contains Figure S1, that illustrates the warm-up procedure that the RSFitOSC program uses. Also included is a brief description of the ice-friction theories of Persson (2015) and Schulson (2015) that we used in Figure 9B. We have also provided a matlab script that will generate these theoretical predictions. Finally, we have included

Corresponding author: R. M. Skarbek, Lamont-Doherty Earth Observatory, Columbia University (rskarbek@ldeo.columbia.edu)

.pdf files containing the plotted results for every oscillation event that we fit, as described in the main text (Datasets S1 – S10).

This submission also includes our datasets (two .csv files and two .mat files). At time of acceptance, these datasets will be archived on the United States Antarctic Data Center.

Text S1.

1. Temperature Dependence of Ice-Granite Friction

Our estimates of the temperature dependence for the steady-state friction coefficient of ice-granite friction follow those of Persson (2015) and Schulson (2015), except altered to account for the granite surface. Here we briefly present the equations that are used to calculate μ in Figure 9B of the main text. Included in the Supplemental Information is a MATLAB program that performs the calculations.

1.1. Persson (2015)

Persson (2015) estimated the friction coefficient of ice-ice sliding by considering the temperature change on the sliding surface as heat is diffused away from the surface of a semi-infinite solid. He assumed that at temperatures near to, but less than the melting temperature T_c, the shear stress would drop rapidly. Following Persson (2015), we assume that the frictional heat flow $J = \tau_m v = J_I + J_G$, where J_I and J_G are the heat flow into the ice and granite, respectively. We further assume that the ice and granite bodies are approximated by semi-infinite solids, in which case the temperature at the sliding interface is

$$T_i = T_0 + 2J_i \left(\frac{t}{\pi H_i}\right)^{1/2}, \quad i = I, G \; , \tag{1}$$

Requiring $T_I = T_G$ yields, $J_G = J_I\sqrt{(H_G/H_I)}$. The heat flow J can now be written as

$$J = \alpha(T_I - T_0) \ , \tag{2}$$

where T_0 is the background/environmental temperature and

$$\alpha = \frac{1}{2}\left(\frac{\pi}{t}\right)^{1/2}\left(H_I^{1/2} + H_G^{1/2}\right) \ . \tag{3}$$

Next, Persson (2015) assumes that a representative contact asperity on the sliding surface survives for some time $t^* = l^*/v$, where l^* is the width of the contact region. Furthermore, he assumes that $\tau_m(T)$ has the form

$$\tau_m = \tau_m^0\left(1 - \frac{T}{T_c}\right)^{\beta} \ . \tag{4}$$

Combining equations (2) – (4) yields an implicit equation for the temperature T at the sliding interface

$$T = T_c + T_0 + \frac{v\tau_m^0}{\alpha}\left(1 - \frac{T}{T_c}\right)^{\beta} \ . \tag{5}$$

Given a sliding velocity v, the friction coefficient can be calculated by solving equation (5) for T, and putting the result into equation (4) to find the shear stress. Finally, $\mu = \tau_m/\sigma_Y$.

1.2. Schulson (2015)

Schulson (2015) performed a calculation similar to that of Persson (2015), and estimated the coefficient of friction by considering the temperature change at a cylindrical asperity surface. He assumed at some proportion η of the asperity surface is coated in a water film, and phenomenologically set this to $\eta = \gamma\ln(v_s/v_t)$, where v_s is the macroscopic sliding rate and v_t is a creep rate at the asperity surface. The friction coefficient is then

$$\mu = [1 - \gamma\ln(v_s/v_t)]\mu_k \ , \tag{6}$$

where μ_k is defined as the ratio of the shear stress necessary to maintain a given creep rate, to the normal stress supported by asperities, taken by Schulson (2015) to be the hardness of ice. Schulson (2015) arrives at the expression [his equations (38) – (41)]

$$\mu_k = C\epsilon^{1/n_2} t^{1/n_1} \exp\left(\frac{Q_2}{n_2 RT} - \frac{Q_1}{n_1 RT}\right) \tag{7}$$

$v_t = 2a/(ft_c)$ where

$$t_c = \left(\frac{L_v \delta}{\Delta T}\right)^2 \left[\left(\kappa_i \rho_i c_p^i\right)^{1/2} + \left(\kappa_g \rho_g c_p^g\right)^{1/2}\right] , \tag{8}$$

where $\Delta T = T - T_c$.

Data Set S1. ds01_C29.pdf: Fits for Experiment C29

Data Set S2. ds02_C30.pdf: Fits for Experiment C30

Data Set S3. ds03_C31.pdf: Fits for Experiment C31

Data Set S4. ds04_C32.pdf: Fits for Experiment C32

Data Set S5. ds05_C33.pdf: Fits for Experiment C33

Data Set S6. ds06_C34.pdf: Fits for Experiment C34

Data Set S7. ds07_C39.pdf: Fits for Experiment C39

Data Set S8. ds08_C40.pdf: Fits for Experiment C40

Data Set S9. ds09_C41.pdf: Fits for Experiment C41

Data Set S10. ds10_C44.pdf: Fits for Experiment C44

Data Set S11. ds11_Fits_All1.mat: Matlab fit structures containing all data and information necessary to reproduce all of the fits for C29 – C33.

Data Set S12. ds12_Fits_All2.mat: Matlab fit structures containing all data and information necessary to reproduce all of the fits for C34 – C44.

Data Set S13. IceGraniteFriction.m: Matlab script for solving equations described in Text S1.

Table S1. ts01_Fits_All.csv: Fitted parameter values and errors for all fits.

Table S2. ts02_Fits_Accepted.csv: Fitted parameter values and errors for accepted fits.

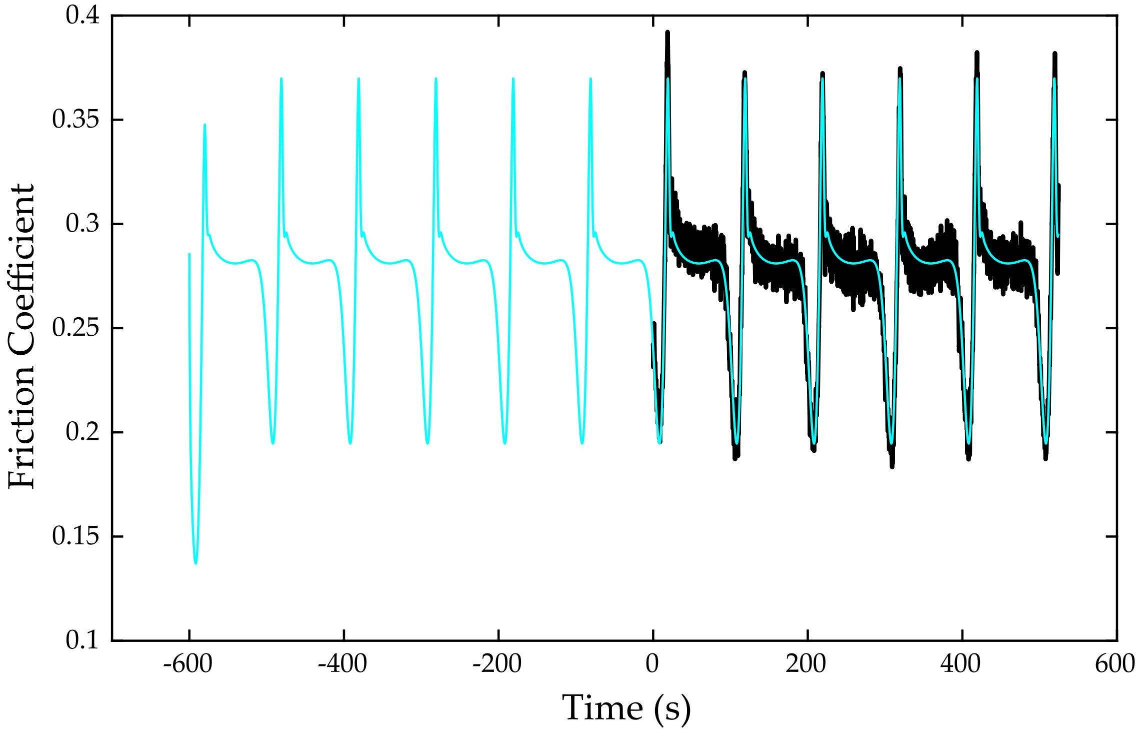

Figure S1. An example of how RSFitOSC runs a number of warm up cycles when optimizing the simulated frictional response (cyan line) to the observed data (black line). In this example, it takes one cycle for the system to enter a steady oscillation; the first cycle is influenced by the initial conditions of the simulation. Only cycles that occur during steady oscillation are used to fit the experimental data. The example here used six warm up cycles, and then the remaining cycles were used to fit the data.